



ELSEVIER

Available online at www.sciencedirect.com

SCIENCE @ DIRECT®

International Journal of Multiphase Flow 32 (2006) 132–157

International Journal of
**Multiphase
Flow**

www.elsevier.com/locate/ijmflow

Numerical modeling and experimental measurements of water spray impact and transport over a cylinder

S.S. Yoon ^{a,*}, P.E. DesJardin ^b, C. Presser ^c, J.C. Hewson ^d, C.T. Avedisian ^e

^a Department of Mechanical Engineering, Korea University, Anamdong, 5-Ga, Sungbukgu, Seoul, 136-713, Korea

^b Department of Mechanical and Aerospace Engineering, University at Buffalo,
State University of New York, NY 14260, United States

^c Chemical Science and Technology Laboratory, National Institute of Standard and Technology, Gaithersburg,
MD 20899-8360, United States

^d Fire Science and Technologies, Sandia National Laboratories, P.O. Box 5800, Albuquerque,
NM 87185-1135, United States

^e Department of Mechanical and Aerospace Engineering, Cornell University, Ithaca, NY 14853, United States

Received 14 October 2004; received in revised form 1 May 2005

Abstract

This study compares experimental measurements and numerical simulations of liquid droplets over heated (to a near surface temperature of 423 K) and unheated cylinders. The numerical model is based on an unsteady Reynolds-averaged Navier–Stokes (RANS) formulation using a stochastic separated flow (SSF) approach for the droplets that includes submodels for droplet dispersion, heat and mass transfer, and impact on a solid surface. The details of the droplet impact model are presented and the model is used to simulate water spray impingement on a cylinder. Computational results are compared with experimental measurements using phase Doppler interferometry (PDI). Overall, good agreement is observed between predictions and experimental measurements of droplet mean size and velocity downstream of the cylinder. © 2005 Elsevier Ltd. All rights reserved.

* Corresponding author. Tel.: +82 2 3290 3350; fax: +82 2 926 9290.

E-mail addresses: ssyoon@sandia.gov, ssyoon@korea.ac.kr (S.S. Yoon).

1. Introduction

The fate of liquid droplets impacting surfaces is of significance to many applications including spray coating, painting, fuel injection in internal combustion engines, spray cooling, and fire-suppression with liquid agents. Over the past decades, a number of studies focusing on single-droplet impact have been conducted (Worthington, 1908; Foote, 1975; Chandra and Avedisian, 1991; Mundo et al., 1995; Pasandideh-Fard et al., 1996; Healy et al., 1996; Mao et al., 1997; Fukumoto et al., 2002; Aziz and Chandra, 2000; Roisman et al., 2002; Kim et al., 2000, 2003; Mehdizadeh et al., 2004; Manzello and Yang, 2004; Gentner et al., 2004), as well as studies focusing on the interaction of entire sprays with surfaces (Mundo et al., 1998; Schmehl et al., 1999). The present work takes advantage of work on single-droplet impact to provide predictive relations for the fate of droplets in a spray impinging on a cylinder with an emphasis on the degree to which the cylinder interferes with the downstream transport of the condensed-phase species. This topic is of particular interest in light of the need to suppress fires in cluttered compartments or rooms. The interaction between the condensed suppressant and various obstructions within a compartment can interfere with the suppressant's distribution. With the phase-out of Halons, fire suppressants with higher boiling points are being employed in total flooding applications, and the issue of spray-clutter interaction takes on greater importance.

When individual droplets impact a surface, several post-impact states can occur. The droplet may elastically rebound, it may stick to the surface, or it may shatter (see Fig. 1). The energetically preferred state depends on the relative surface and kinetic energies along with the viscous dissipation of energy during the impact process. At low droplet kinetic energies, either “sticking” or elastic “rebounding” occurs, depending on the surface energy relative to the dissipated energy. At high droplet kinetic energies, splashing (or shattering) occurs when the kinetic energy is distributed among smaller droplets with a higher overall surface energy (relative to the original droplet). These results have been derived from a large number of experimental and computational studies of isolated droplets. The earliest work in this area dates back to Worthington (1908). Early numerical simulations of droplet impact, where only inertial and viscous forces were considered, include Harlow and Shannon (1967) and following works. The importance of surface tension was noted

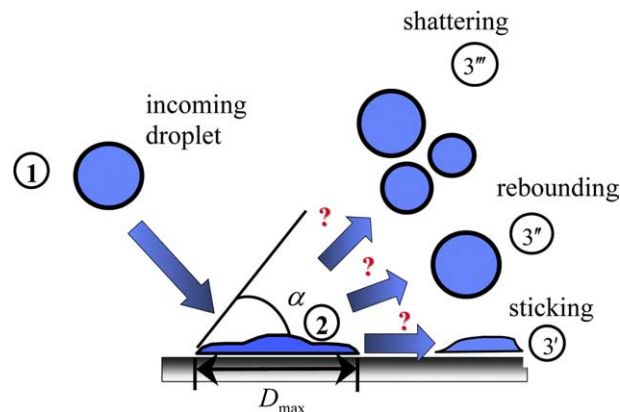


Fig. 1. Configuration states during droplet impact consisting of: (1) pre-impact; (2) impact and (3) post-impact (i.e., sticking, rebound, or shattering).

early in numerical studies like those of Foote (1975), where the inclusion of surface tension allows droplet rebound, as experimentally observed by Wachters and Westerling (1966). A simple energy balance was introduced by Ford and Furmidge (1967) and more recently by Chandra and Avedisian (1991) to relate the total energy of the pre-impact condition to the maximum spread of a single droplet following impact; this simple model was shown to be in reasonable agreement with experimental results in this work, and a number of similar works have offered refinements on this basic energy balance model. Implicit in this model is an estimate of the viscous dissipation occurring while the droplet spreads. Chandra and Avedisian (1991) assumed a linear velocity profile across the entire droplet height while Pasandideh-Fard et al. (1996), based on analysis of their numerical simulations, put forth a model for viscous dissipation that was based on stagnation flow. Mao et al. (1997) points out that the choice of model depends on the boundary layer thickness and it appears that both models are relevant at different times. Mao et al. (1997) also continued the energy balance to a third state where the excess surface energy at the point of maximum spread could cause the droplet to rebound off the surface; this last state appears to be most likely when the droplet contact angle is large, as for example when the Leiden frost temperature is exceeded, and droplet rebound was observed under these conditions by Chandra and Avedisian (1991). Mundo et al. (1995) investigated the critical characteristic impingement parameter (K_{crit}), which distinguished the “shattering” regime from the sticking and rebounding regimes. Fukumoto et al. (2002) suggested an improved model for the characteristic impingement parameter relative to that of Mundo et al. (1995). The experimental and analytical investigations of Aziz and Chandra (2000), Kim et al. (2000, 2003), Mehdizadeh et al. (2004) indicated that the droplet impact is governed essentially by the surface tension instability and, therefore, the effect of viscosity is of little importance.

Several groups have studied the impingement of a spray on flat surfaces. Schmehl et al. (1999), Park and Watkins (1996), Bai et al. (2002) developed numerical formulations that were based on the experimental work of Wachters and Westerling (1966). Mundo et al. (1998) carried out both experimental measurements and developed a numerical formulation that was based on the model of Wang and Watkins (1993), but included shattering criteria (see Mundo et al., 1995) for their spray simulation. Inclusion of the shattering criteria resulted in a smaller overall droplet size for their numerical prediction than predicted by Wang and Watkins (1993), and better agreement with the experimental data.

The current work examines the transport of water droplets around a circular cylinder. This problem is a simplification of the more challenging problem of modeling water spray fire suppression in cluttered environments (Presser et al., 2001, 2002). The objective of this study is to develop a simplified phenomenological droplet impact model for use in fire suppression applications that is suitable for numerical simulation of sprays involving a multitude of droplets of varying size and velocity, and to validate this model using experimental measurements of droplet size and velocity.

2. Experimental apparatus

2.1. Experimental facility

A schematic of the experimental facility is shown in Fig. 2. The salient features of the experimental apparatus and operating conditions are presented for brevity. The facility is oriented so

that the flow issues horizontally to allow for the collection of liquid agent that drips off the cylinder, and prevent liquid droplets downstream of the obstacle from falling back upstream into the oncoming flow. The agent used in the present study was water, supplied through a 60° solid-cone, pressure-jet atomizer with a higher concentration of droplets in the center of the spray cone. An octagon-shaped clear plastic insert (with a wall thickness of 6 mm, length of 610 mm, and major and minor axes of 760 mm and 560 mm) was used as a boundary condition. The plastic insert, along with a front face that supported the inlet passages for the water and air, and a back face that supported the exhaust passage, served to form a closed system. For the present experiments, the incoming air (supplied at 265 kg/h) was directed entirely through a distributor plate with steel wool, a circular cross-sectional area of honeycomb to straighten the airflow (203 mm in diameter, and 51 mm thick with 3 mm size cells), and then through a wire mesh screen, as illustrated in Figs. 2 and 3. The honeycomb and wire mesh screen were co-positioned around the injector (see Fig. 3).

Grid-generated turbulence was imposed on the air stream to provide a well-controlled turbulence flow field and specified turbulence intensity for the modeling effort. This was accomplished by placing a square layer of wire mesh screen (with dimensions of 229 mm width by 330 mm length, 3.2 mm wire thickness, and 13 mm size cells) 25 mm downstream of the honeycomb. The rationale for this arrangement is given in detail elsewhere (Presser et al., 2001, 2002). Briefly, the grid was placed downstream of any jetting of the airflow exiting the honeycomb. The face of the atomizer was placed flush with the upstream side of the grid, and centered within one mesh cell so that the liquid spray would be unimpeded by the grid. The mean streamwise air velocity was 4.0 m/s. The turbulence intensity was estimated to be approximately 8 m/s. The turbulent integral and Kolmogorov length scales were estimated to be approximately 1.3 cm (approximated by the characteristic dimension of the grid mesh size) and 150 μm (see Pope, 2000; Wells and Stock, 1983; Snyder and Lumley, 1971), respectively, representing the range of length scales

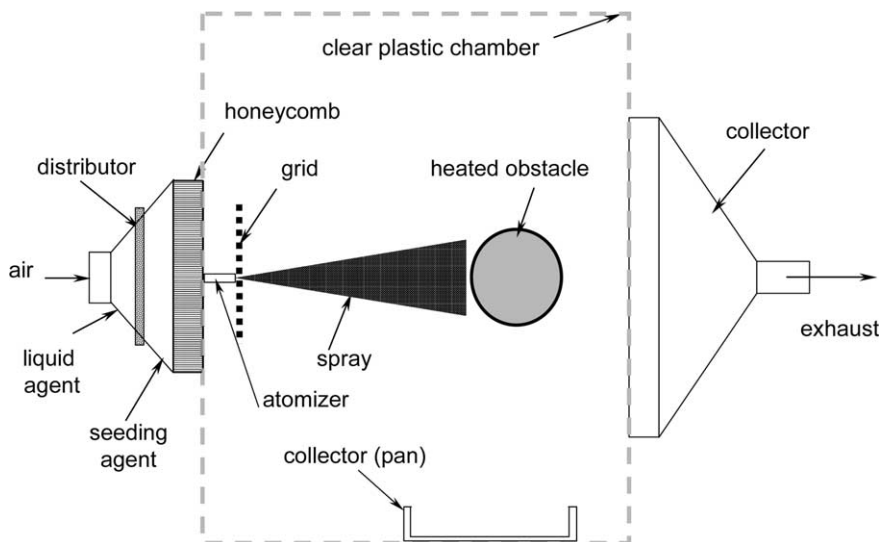


Fig. 2. Schematic of the experimental arrangement for the droplet-laden, grid-generated turbulent flow field.

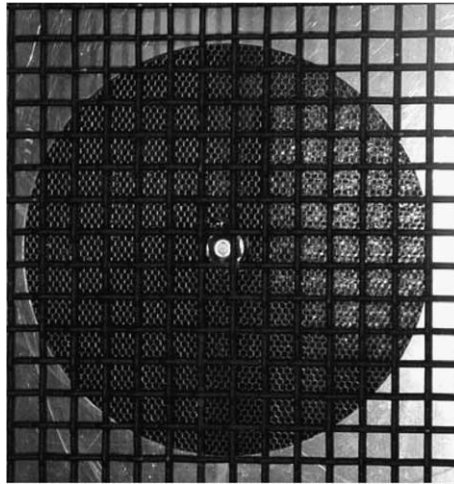


Fig. 3. Photograph of liquid atomizer placement in relation to the honeycomb and wire mesh screen.

associated with this flow field. A stepper-motor-driven traversing system translated the entire assembly, and permitted measurements of the flow field properties at selected locations downstream of the injector and around the obstacle.

2.2. Obstacle characteristics

The obstacle was an aluminum cylinder with a diameter of approximately 29.2 mm and a length of 305 mm (see Fig. 4). Its diameter was larger than the integral length scale of turbulence. A hole (13 mm in diameter) was bored through the center to accommodate a 250 W cartridge heater (13 mm in diameter and 76 mm in length). The rod was split along its axis into two halves to permit 1 mm deep channels to be milled along one segment for placement of five K-type thermocouples (Inconel sheathed, ungrounded, 0.8 mm in diameter, and 305 mm long). The thermocouples were placed in a cross-pattern in the center of the rod (each separated by a distance along the surface of 6.4 mm, with the thermocouple junctions placed about 3.2 mm of the surface from within bored holes at each location). The central thermocouple was used for temperature control of the

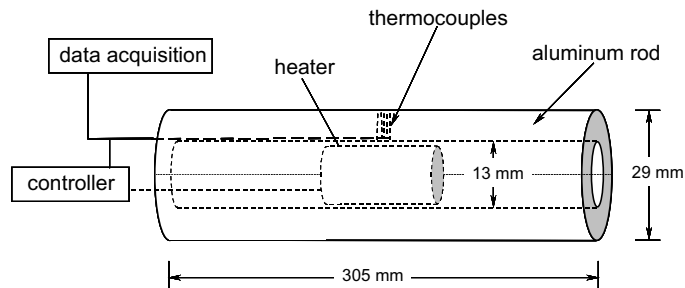


Fig. 4. Schematic of the cylinder with the installed cartridge heater.

heater, which was positioned behind the thermocouples. Estimation of the measurement uncertainty is determined from statistical analysis of a series of replicated measurements (referred to a Type A evaluation of uncertainty), and from other means other than statistical analysis (referred to Type B evaluation of uncertainty) (Taylor and Kuyatt, 1994). The expanded uncertainty for the temperature was 275.8 K, calculated as $2u_c$ (representing a level of confidence of 95%), where u_c is the combined standard uncertainty. The value for u_c was estimated statistically by $sn^{-1/2}$, where s is the standard deviation of the mean and n is the number of samples (Type A uncertainty), and from the manufacturer uncertainty (Type B uncertainty).

2.3. Phase Doppler interferometer

Phase Doppler interferometry (PDI) (Bachalo and Houser, 1984) has been used to characterize sprays in areas such as liquid fuel spray combustion, coal slurry combustion, coatings, pesticides, and fire suppression. PDI is an extension of laser Doppler velocimetry that measures droplet size as well as velocity. Phase Doppler techniques involve creating an interference pattern in the region where two laser beams intersect, and results in a region consisting of alternating light and dark fringes. The region where the laser beams intersect is called the probe volume or sample volume. Due to the interference pattern, a droplet passing through the probe volume scatters light that exhibits an angular intensity distribution, which is characteristic of the size, refractive index, and velocity of the droplet. For a droplet with known refractive index, the size and velocity can be determined by analyzing the scattered light collected with several photomultiplier tubes.

The PDI is a single-point (or spatially resolved) diagnostic instrument in that it obtains information about the spray at a single point in space. Only by moving the probe volume (or, equivalently, the spray) can one map out the spatial distribution of the spray characteristics. The PDI is also a single-droplet instrument in that information is obtained for only one droplet at a time. This offers advantages over integrating techniques because the characteristics of a particular droplet (size, velocity, etc.) can be recorded and the data can be separated into classes (size classes, velocity classes) to further characterize the spray.

The experiments were conducted using a two-component phase Doppler interferometer with a real-time signal analyzer. Again, only the main features of the PDI arrangement are presented by brevity. A 5 W argon ion laser operating in multi-line mode was used as the illumination source. The blue (wavelength = 488 nm) and green (wavelength = 514.5 nm) lines of the argon ion laser were separated by beam conditioning optics, and focused by the transmitting optics to intersect and form the probe volume. The front lens on the transmitter has a focal length of 500 mm. The green and blue beams have a beam separation distance of 39.9 mm and 40.2 mm, fringe spacing of 6.45 μm and 6.07 μm , and beam waist of 164 μm and 155 μm , respectively. Frequency shifting is set at 40 MHz. The receiver was located at a scattering angle, θ , of 30° measured from the direction of propagation of the laser beams. To accommodate the horizontal orientation of the experimental apparatus, the transmitter and receiver were positioned in a vertical plane, as shown in Fig. 5. Due to the large size of the receiver, the transmitter was positioned with the laser beams angled at 30° to the cylinder, which required correction of the cross-stream velocity by dividing its magnitude by the cosine of the angle. The front lens on the receiver had a focal length of 1000 mm. Hardware coincidence, which requires that droplets be detected on both PDI channels simultaneously to be validated, was used as an additional validation criterion for all

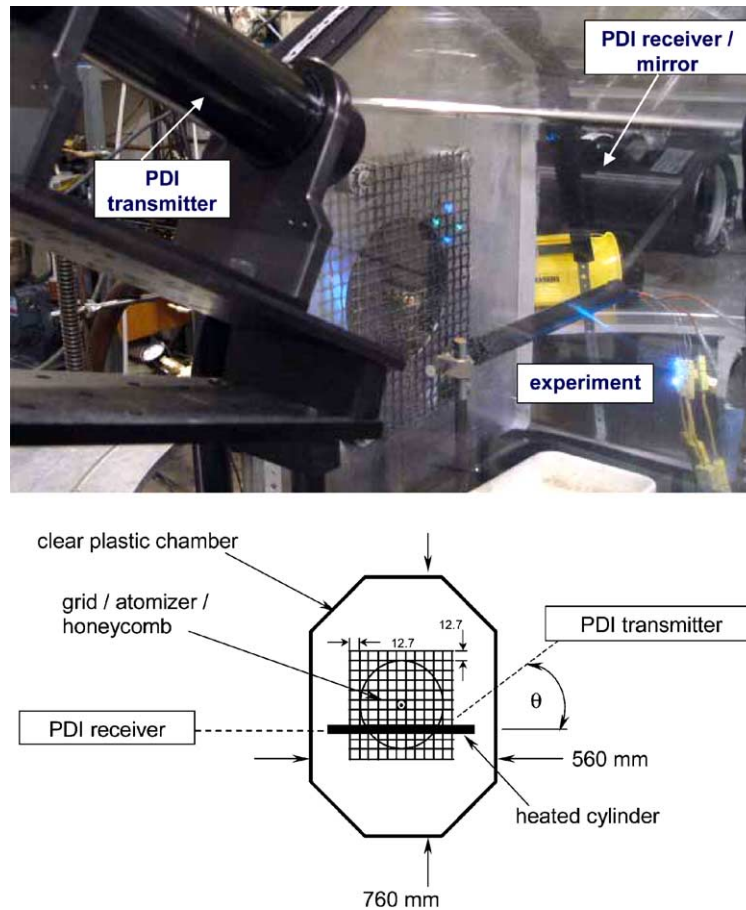


Fig. 5. View and schematic of the experimental arrangement with the laser from the phase Doppler interferometer.

measurements. Intensity validation (to remove droplets whose scattered light intensities are too low and high, and result in erroneous phase shifts and droplet sizes), and probe volume corrections (to account for droplets of varying size traveling through different sections of the Gaussian beam profile) were carried out to optimize the quality of the measurements. The measurements were carried out at several radial (z , cross-stream) positions and over a range of axial (x , streamwise) positions upstream and downstream of the cylinder.

3. Computational model

3.1. Modeling background

Numerical simulations are conducted using Sandia's fire field modeling code VULCAN, which has been extended to handle the dilute multiphase flow physics found in evaporating and reacting sprays (DesJardin and Gritzo, 2002; Yoon et al., 2004). The spray model is coupled with the

Navier–Stokes solver, based on a Reynolds-averaged Navier–Stokes (RANS) formulation employing a standard $k-\varepsilon$ turbulence closure model (Jones and Launder, 1972). The gas-phase flow is calculated on a Eulerian staggered Cartesian grid using the SIMPLEC method (Patankar, 1980).

The droplet phase evolves using a Lagrangian approach based on the stochastic separated flow model (Faeth, 1983, 1987). Evolution equations for collections of droplets with similar sizes and initial conditions, denoted as parcels, are used to reduce computational cost. The parcels are advanced under the influence of modeled turbulent fluctuations in the gas-phase properties. The momentum equation for a small rigid sphere in a nonuniform flow of Maxey and Riley (1983) is used. The drag model of Chhabra et al. (1999) and the correlation by Ganser (1993), which is similar to the model of Helenbrook and Edwards (2002), is used. Evaporation is modeled using a thin skin model with standard convective correlations for heat and mass transfer. Further details may be found in DesJardin and Gritzo (2002).

3.2. Phenomenological droplet impact model

A droplet impact model based on the work of DesJardin et al. (2002, 2003) is used in this study. The model is formulated using simple mass and energy conservation principles at three thermo-physical droplet states (shown in Fig. 1). State (1) corresponds to the pre-impact state where the droplet is assumed to be spherical in shape and the mass and energy of the droplet can be expressed as

$$\begin{aligned} m &= \rho^{(1)} \pi D^{(1)3} / 6 \\ E &= E_S^{(1)} + E_{KE}^{(1)} = \sigma^{(1)} \pi D^{(1)2} + \rho^{(1)} \pi D^{(1)3} |U^{(1)}|^2 / 12 \end{aligned} \quad (1)$$

where, E_{KE} and E_S denote the droplet kinetic and surface energies expressed in terms of the droplet diameter D , the droplet density ρ , the magnitude of droplet mean axial (streamwise) velocity $|U|$, and the liquid surface tension σ . The superscript (1, 2, 3) notation indicates properties of the droplet before, during, and after impact, respectively. At impact state (2), the droplet is assumed to be roughly pancake-shaped, with a maximum diameter equal to D_{\max} . At this state, the kinetic energy of the droplet is negligible and results in only a surface energy contribution to the total energy of the droplet (Ford and Furnidge, 1967),

$$E_S^{(2)} = \frac{\pi}{4} D_{\max}^2 (1 - \cos \alpha) \sigma \quad (2)$$

where α is the contact angle and is defined as the intersection of the tangent line at the liquid–vapor interface with the wall (see Fig. 1).

The droplet diameter at state (2), when maximum deformation has taken place and the kinetic energy is negligible, may be determined through an energy balance by equating the pre-impact energy of the droplet at state (1) to the sum of the surface energy at state (2) and the lost energy due to viscous dissipation.

$$E_S^{(1)} + E_{KE}^{(1)} = E_S^{(2)} + W_{\text{diss}} \quad (3)$$

In Eq. (3), W_{diss} is the energy dissipated by viscous forces as the droplet deforms from state (1) to (2). The viscous work is estimated following Pasandideh-Fard et al. (1996) as

$$W_{\text{diss}} \cong \rho\pi|U_i|^2 D^3 \beta_{\text{max}}^2 / (3\sqrt{Re}) \tag{4}$$

where $|U_i|$ is the magnitude of droplet impact velocity, Re is the droplet Reynolds number ($Re = |U_i|D/\nu$), $\nu (= \mu/\rho)$ is the liquid kinematic viscosity, ρ is the liquid density, μ is the liquid viscosity, and β_{max} is defined as the ratio of the maximum droplet diameter at state (2) to its original diameter, i.e., $\beta_{\text{max}} = D_{\text{max}}/D$. Substituting this expression for work along with the surface and kinetic energy definitions of Eqs. (1), (2), (4) into Eq. (3) provides the following analytical result for β_{max} (Pasandideh-Fard et al., 1996):

$$\beta_{\text{max}} = \sqrt{\frac{12 + We}{3(1 - \cos \alpha) + 4\left(\frac{We}{\sqrt{Re}}\right)}} \tag{5}$$

where We is the Weber number, $We = \rho D|U_i|^2/\sigma$. Once β_{max} is determined, the energy at state (2) is known and is used to determine the energy at state (3). Fig. 6 shows that β_{max} (solid lines) is always greater than unity and its value decreases as the contact angle increases.

At state (2), the energy of impact is expended and the droplet spreads over the surface with viscous losses. The state at (2) is not necessarily that which minimizes the droplet surface energy, however, the droplet tends to rebound to minimize the surface energy. During this process, additional viscous dissipation may occur, but if there is sufficient surface tension the droplet may return to its spherical form and leave the surface.

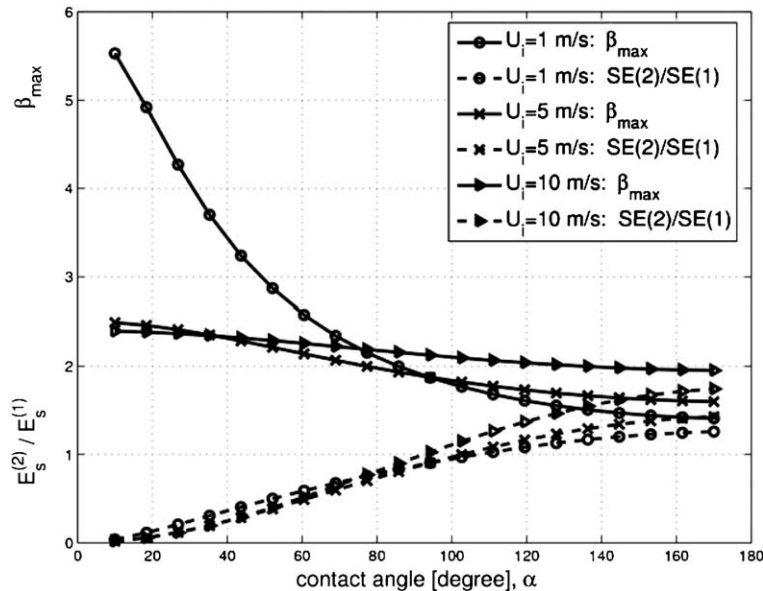


Fig. 6. Variation of the ratio between the surface energy at state (2) and that of (1) (dash-lines) and β_{max} (solid-lines) with contact angle, α , for different droplet impact velocities of $U_i = 1$ m/s, 5 m/s, and 10 m/s.

At state (3), one of three events is assumed to occur – either droplet sticking (3'), rebounding (3''), or shattering (3'''). At high initial kinetic energies, droplet shattering (or splashing) will occur if the characteristic impingement parameter, K , exceeds its critical value, $K_{\text{crit}} = 57.7$ (Mundo et al., 1995), expressed in terms of the Ohnesorge number ($Oh = \sqrt{We}/Re$),

$$K = Re^{1.25} Oh = We^{0.5} Re^{0.25} \quad (6)$$

If $K > K_{\text{crit}}$, the droplet shatters (splashes). If $K < K_{\text{crit}}$, the droplet either rebounds or sticks to the surface. The critical value, $K_{\text{crit}} = 57.7$ of Mundo et al. (1995) is applicable for a wide range of substrate roughness (i.e., $10^{-3} < \gamma < 10^0$ where γ is the dimensionless surface roughness that is defined by Mundo et al., 1998). However, K_{crit} increases with decreasing surface roughness since an impacting liquid droplet can spread further on a smoother surface before it shatters. Mundo et al. (1998) noted that K_{crit} can increase up to $K_{\text{crit}} \sim 140$. Mao et al. (1997) showed that K_{crit} can increase up to $K_{\text{crit}} \sim 152$ for a water droplet on a paraffin wax surface (see Fig. 7(c) of Mao et al., 1997).

For velocities for which $K < K_{\text{crit}}$, the droplet is assumed to either stick or rebound off of the surface. An expression for the droplet kinetic energy at state (3'') (rebound) may be determined by considering overall energy conservation from states (2) to (3''), assuming an adiabatic surface.

$$E_{\text{KE}}^{(3'')} = E_{\text{S}}^{(2)} - E_{\text{S}}^{(3'')} - W_{\text{rebound}} \quad (7)$$

In Eq. (7), W_{rebound} is the work required for the droplet to rebound from a pancake to a spherical shape. Since the surface tension energy at state (3'') is the same as state (1) then the kinetic energy at state (3'') can be determined if W_{rebound} is known. To the authors' knowledge, a relation

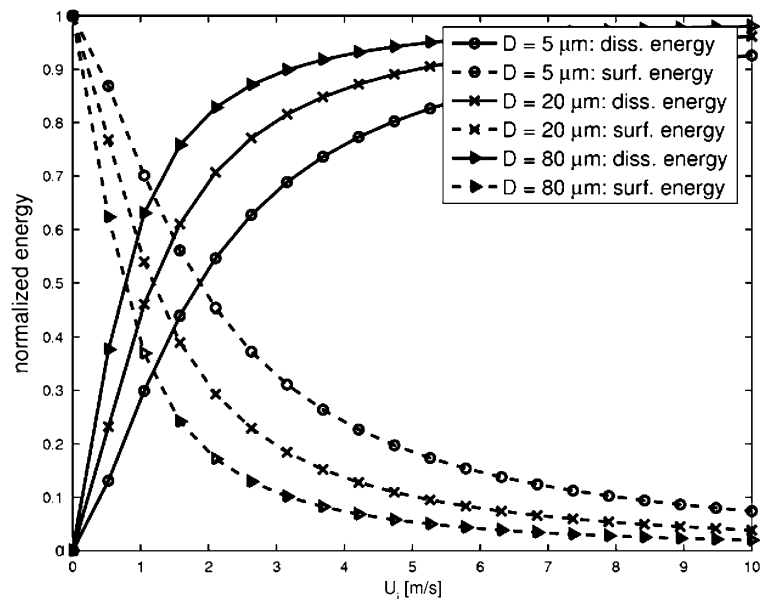


Fig. 7. Variation of the normalized surface and dissipated energies at state (2) with impact velocity for water droplet diameters of $D = 5 \mu\text{m}$, $20 \mu\text{m}$, and $80 \mu\text{m}$. Note that the contact angle is $\alpha = 27^\circ$.

for W_{rebound} is not available. However, recent experimental studies of molten metal droplets by Aziz and Chandra (2000) suggest that if the surface energy at state (2) is greater than the energy dissipated during impact, the droplet will rebound; otherwise the droplet will stick. This simple criterion for droplet rebounding is employed by assuming that if $E_S^{(2)} < W_{\text{diss}}$, the droplet sticks to the surface and the parcel is removed from the calculation (i.e., no dripping is taken into account). If $E_S^{(2)} > W_{\text{diss}}$, the droplet is assumed to rebound and the velocity components of the droplet are adjusted to satisfy the known kinetic energy at state (3''). As an example, the variation of the normalized $E_S^{(2)}$ and W_{diss} for water droplets of different size (i.e., $D = 5 \mu\text{m}$, $20 \mu\text{m}$, and $80 \mu\text{m}$) is given in Fig. 7 with respect to impact velocity, using Eqs. (2) and (4). In Fig. 7, the surface energy and dissipated work are normalized by the total energy of the droplet at state (1). Droplet rebounding occurs at low impact velocities (i.e., $U_i = 1.86 \text{ m/s}$, 1.17 m/s , and 0.74 m/s for $D = 5 \mu\text{m}$, $20 \mu\text{m}$, and $80 \mu\text{m}$, respectively, which are the cross-points where the surface and dissipated energies meet) when the surface energy of the droplet at state (2) exceeds the amount of work required to deform the droplet. The difference in these quantities approximates the amount of kinetic energy of the droplet at state (3''), $E_{\text{KE}}^{(3'')}$.

$$E_{\text{KE}}^{(3'')} = E_S^{(2)} - W_{\text{diss}} \quad (8)$$

Substituting Eq. (8) into Eq. (7) and solving for results in the following expression for the work from droplet rebounding

$$W_{\text{rebound}} = W_{\text{diss}} - E_S^{(3'')} \quad (9)$$

which implies that the work for droplet rebounding is modeled as the difference between the work to initially deform the droplet minus the surface energy at state (3''). This expression which is derived from the experimental observations of Aziz and Chandra (2000) is ad hoc. Future efforts will be directed to examine the limitations of this approximation. Once the kinetic energy at state (3'') is known then the magnitude of the droplet rebounding velocity ($|\bar{u}_{\text{reb}}|$) may be determined as

$$|\bar{u}_{\text{reb}}| = \sqrt{\frac{2E_{\text{KE}}^{(3'')}}{\pi \rho D^3}} \quad (10)$$

Specification of the rebounding velocity components would, in general, require consideration of momentum conservation of the droplet. This, in turn, requires detailed knowledge of the forces exerted on the droplet over the time duration of impact. Thus, the momentum loss may be determined for each velocity component, but is often difficult to obtain. A simplification is introduced that specifies the components of velocity after impact to be proportional to the velocity components before impact with respect to a coordinate system locally aligned to the impact surface (see Fig. 8). This assumption results in equal incident angles for pre-impact and post-impact trajectories. The incident angle is defined in this context as the angle between the surface normal and droplet trajectory. To enforce this condition, the Cartesian velocity components of the droplet are first decomposed into a coordinate system aligned with the surface of impact, $(\hat{e}_{\parallel}, \hat{e}_{\perp 1}, \hat{e}_{\perp 2})$, as shown in Fig. 8. The velocities, u_{\parallel} , $u_{\perp 1}$ and $u_{\perp 2}$ are the components of the droplet velocity in this new coordinate system decomposed into components parallel to the surface area vector and perpendicular to it, respectively, using the following coordinate transformation:

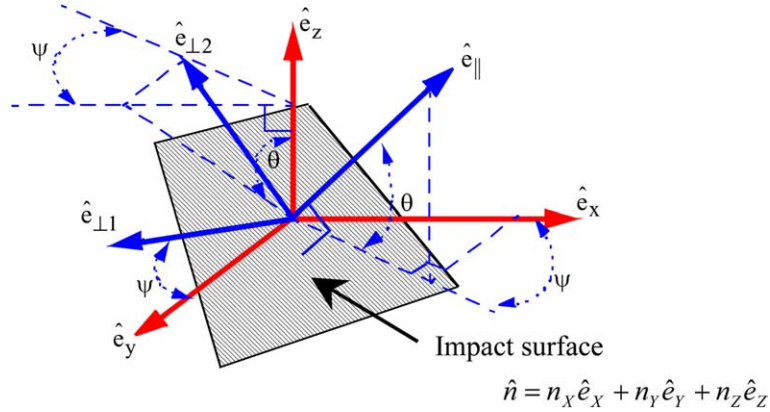


Fig. 8. Relationship between the impact surface and Cartesian coordinate systems.

$$\begin{Bmatrix} u_{\parallel}^{(1)} \\ u_{\perp 1}^{(1)} \\ u_{\perp 2}^{(1)} \end{Bmatrix} = \underline{T} \begin{Bmatrix} u^{(1)} \\ v^{(1)} \\ w^{(1)} \end{Bmatrix} = \begin{bmatrix} \cos \theta \cos \psi & \cos \theta \sin \psi & \sin \theta \\ -\sin \psi & \cos \psi & 0 \\ -\sin \theta \cos \psi & -\sin \theta \sin \psi & \cos \theta \end{bmatrix} \begin{Bmatrix} u^{(1)} \\ v^{(1)} \\ w^{(1)} \end{Bmatrix} \quad (11)$$

where the directional angles θ and ψ are defined as

$$\begin{aligned} \sin \theta &= \hat{e}_{\parallel} \cdot \hat{e}_z \\ \cos \theta \sin \psi &= \hat{e}_{\parallel} \cdot \hat{e}_y \\ \cos \theta \cos \psi &= \hat{e}_{\parallel} \cdot \hat{e}_x \end{aligned} \quad (12)$$

The rebound velocity components in the transformed system are then obtained using the following relations,

$$\begin{aligned} u_{\parallel}^{(3'')} &= -f u_{\parallel}^{(1)} \\ u_{\perp 1}^{(3'')} &= f u_{\perp 1}^{(1)} \\ u_{\perp 2}^{(3'')} &= f u_{\perp 2}^{(1)} \end{aligned} \quad (13)$$

where f is a decrement factor, defined as

$$f^2 = E_{KE}^{(3'')} / E_{KE}^{(1)} \quad (14)$$

Employing Eqs. (13) and (14) results in post-impact velocities that have the same kinetic energy as that determined from Eq. (8). Once the velocities at state (3'') are known from Eq. (13), the velocities for the impact plane coordinate system are transformed back to a Cartesian system using the following inverse transformation:

$$\begin{Bmatrix} u^{(3'')} \\ v^{(3'')} \\ w^{(3'')} \end{Bmatrix} = \underline{T}^{-1} \begin{Bmatrix} u_{\parallel}^{(3'')} \\ u_{\perp 1}^{(3'')} \\ u_{\perp 2}^{(3'')} \end{Bmatrix} = \begin{bmatrix} \cos \theta \cos \psi & -\sin \psi & -\sin \theta \cos \psi \\ \cos \theta \sin \psi & \cos \psi & -\sin \theta \sin \psi \\ \sin \theta & 0 & \cos \theta \end{bmatrix} \begin{Bmatrix} u_{\parallel}^{(3'')} \\ u_{\perp 1}^{(3'')} \\ u_{\perp 2}^{(3'')} \end{Bmatrix} \quad (15)$$

The partitioning of the post-impact velocities, using Eqs. (11)–(15), is not unique and other approaches could be pursued that would require more detailed knowledge of the impact dynamics. For this study, the details of exactly how the kinetic energy is distributed among the velocity components is not critical since the inertia associated with the kinetic energy at state (3'') is much smaller than local aerodynamic drag forces.

3.3. Computation details

We assume that the aluminum cylinder surface has a regular surface roughness profile and, thus, the surface roughness remains within $R_x \approx 2.22 \mu\text{m} \pm 10\%$ (Moita and Moreira, 2003). The wettability of the surface remains within $\alpha < 90^\circ$ for the isothermal process between the impacting droplet and the substrate. The measurement of Pasandideh-Fard et al. (1996), $\alpha = 27^\circ$, is adopted for our numerical simulation. The contact angle of a droplet on a hot surface is generally greater than 90° (Aziz and Chandra, 2000; Harvie and Fletcher, 2001). However, the wettability increases as droplets accumulate on the cylinder surface (i.e., at steady-state, droplets are essentially impacting a liquid film rather than a dry surface), and in such cases, the contact angle is reduced even though the surface is hot (Mundo et al., 1998). For the case of liquid droplet impinging on a hot surface, the contact angle $\alpha = 67^\circ$ is extrapolated to account for the hot surface and liquid film effects, based on our experimental observations and the measurements of Bernardin et al. (1997), Mundo et al. (1998), Aziz and Chandra (2000), Harvie and Fletcher (2001).

All simulations are run for two physical seconds on a $0.58 \text{ m} \times 0.30 \text{ m} \times 0.30 \text{ m}$ ($-0.18 \text{ m} < x < 0.4 \text{ m}$, $-0.15 \text{ m} < y < 0.15 \text{ m}$, $-0.15 \text{ m} < z < 0.15 \text{ m}$) domain to allow for initial flow transients to be removed from the computational domain, and to collect data for determining time-averaged statistics. A constant air velocity, $u_\infty = 4.0 \text{ m/s}$, was specified at the inlet which modeled the grid-generated turbulence of the wire mesh screen (see Section 2.1) with the specified turbulent kinetic energy of 0.194 J/kg and a turbulent kinetic-energy dissipation rate of 0.470 J/kg s for the reasons stated by Presser et al. (2001). Constant pressure boundary conditions were applied at all other boundaries. When adopting u_∞ as a characteristic velocity, the flow Reynolds number based on the cylinder diameter is $Re_{\text{flow}} = u_\infty D_{\text{cyl}}/v_{\text{air}} = 7584$. A $70 \times 50 \times 50$ Cartesian grid is employed (having a total number of computational nodes of 175,000) with grid stretching employed to enhance the resolution around the cylinder. A grid sensitivity study revealed that the results are grid independent for the resolution chosen. Each simulation is conducted by running an unsteady RANS simulation and collecting ensemble statistics after an initial time of $t = 0.5 \text{ s}$ (see Fig. 9) when the flow attains a statistical stationary state. Fig. 9 presents a typical early-time development of the two-phase flow. Statistics are collected from $t = 0.5 \text{ s}$ to 2.0 s at intervals of 0.0002 s ; thus averages represent 7500 samples per control volume collected during 1.5 s .

The spray injection is initiated at location $x = -0.18 \text{ m}$ and $y = z = 0$. To represent conditions at the nozzle exit, assumed droplet size and velocity distributions are often used. There are many known droplet size distribution functions such as normal, log-normal, root-normal, Rosin–Rammler, Nukiyama–Tanasawa, and log-hyperbolic (Babinsky and Sojka, 2002). We chose the Rosin–Rammler distribution since this distribution is shown to have merits in modeling the initial conditions (Yoon et al., 2004). The boundary of the numerical simulation is initiated at the nozzle position. Measurement of droplet size and velocity immediately downstream of the nozzle is difficult to obtain experimentally because of the high droplet number concentration. A precise initial

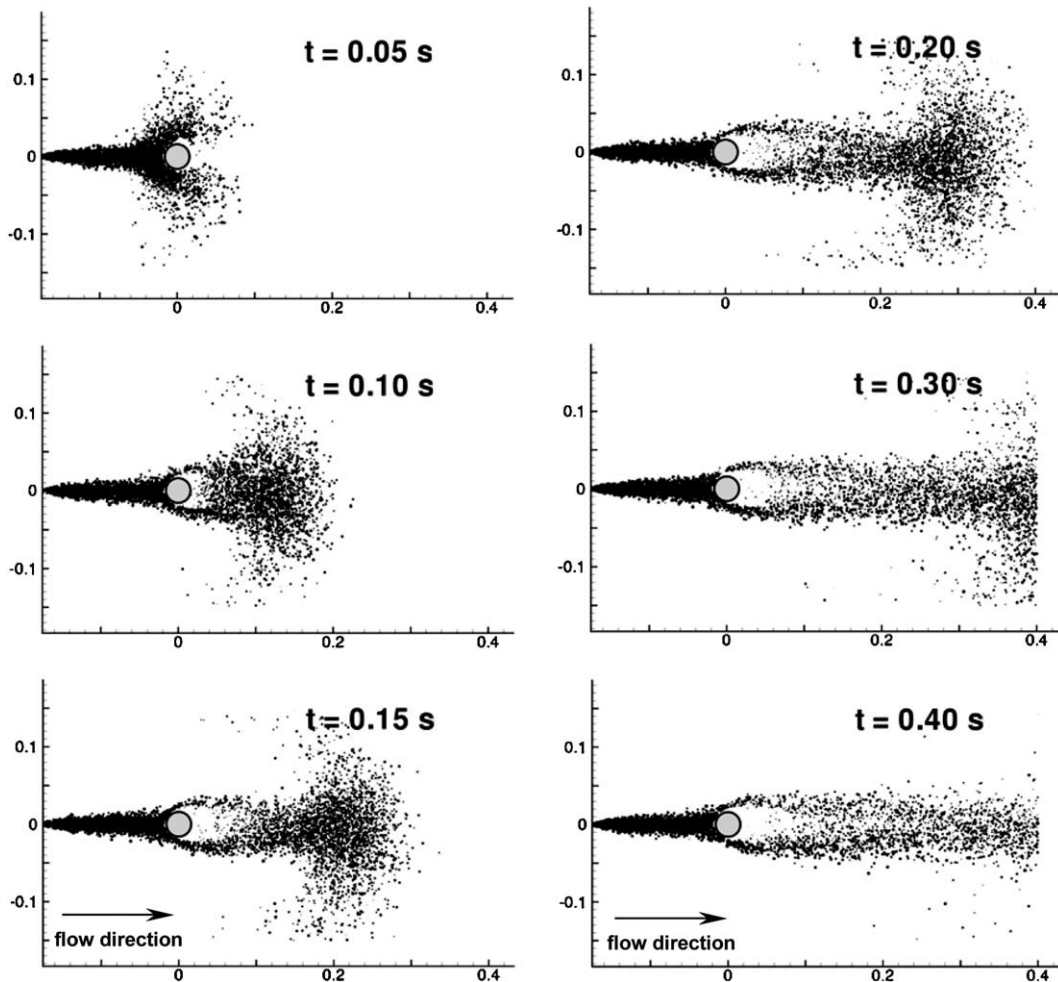


Fig. 9. Evolution of the droplet transport process over the cylinder.

condition for the numerical simulations is therefore not available from the experiments. As an alternative, a Rosin–Rammler distribution for droplet size was assumed with the input fitting parameters (X and q) chosen to best match the experimentally measured droplet Sauter mean diameter, D_{32} , upstream of the cylinder at $x = -50$ mm. The initial spray angle of 20° was chosen to match the experiments and the initial velocity of each injected droplet was chosen to match the mass flow rate of $\dot{m} = 8.41 \times 10^{-4}$ kg s $^{-1}$ in the nozzle. Several runs were conducted to match the measured droplet diameter upstream of the cylinder. Fig. 10 shows only three of many runs that were conducted to match the initial conditions from the experimental data. Fig. 10(a) presents the variation of D_{32} with downstream location at a radial (cross-stream) location of 20 mm from the cylinder centerline with $X = 28$ μm , which defines the center of the distribution, and for $q = 2, 3$ and 4, which define the width of the distribution. The closest agreement to the experimental data is obtained for the case for $q = 3$, corresponding to an initial particle diameter of $D_{10} = 25$ μm ,

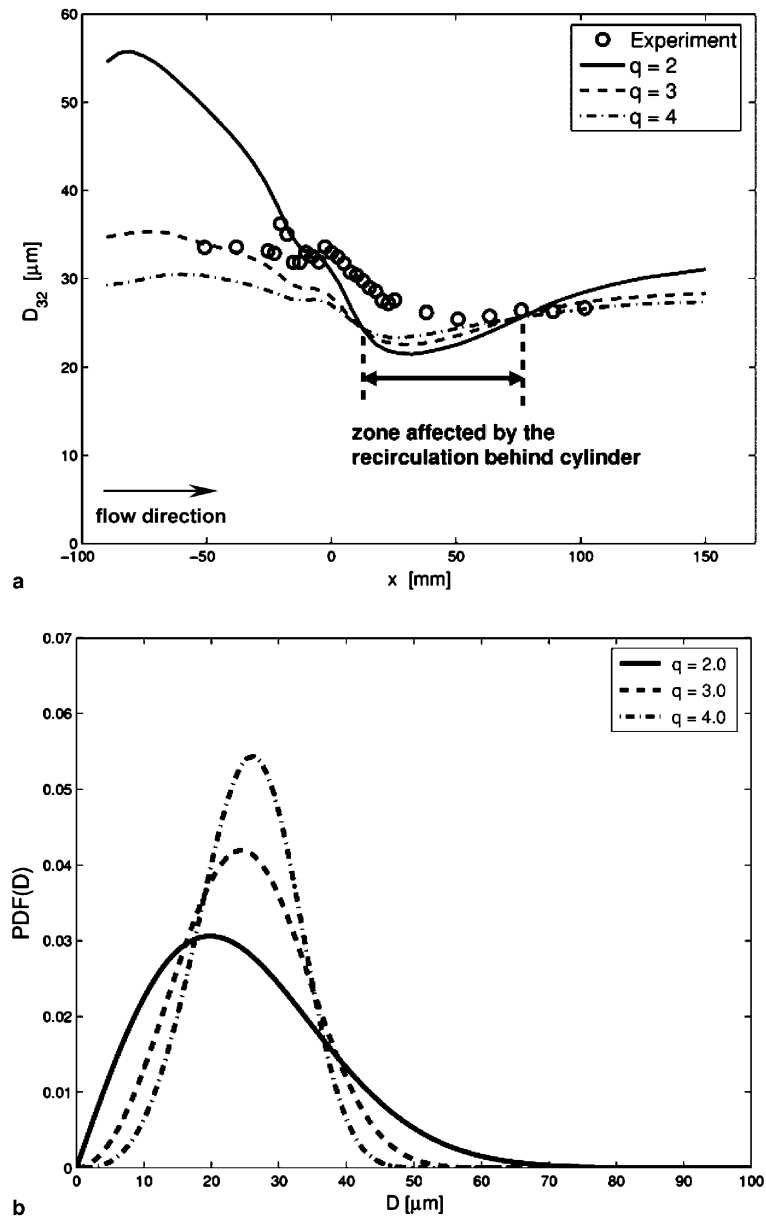


Fig. 10. Variation of the: (a) Sauter mean diameter, D_{32} , with axial (or streamwise) locations at the radial (or cross-stream) location of $z = 20$ mm and (b) initial droplet size distribution, using the Rosin–Rammler distribution function. Note the computational results are from the unheated cylinder case.

where $D_{10} = X\Gamma(1/q + 1)$ and Γ represents the Gamma function (Yoon et al. (2004)). The corresponding Sauter mean diameter, D_{32} , can be found using the following equation: $D_{32} = X\Gamma(3/q + 1)/\Gamma(2/q + 1) = 31.02 \mu\text{m}$. Fig. 10(b) presents the probability distribution function (PDF) of D_{32} for the same cases, and indicates that decreasing the value of q results in a

larger number of smaller and larger droplets being injected. The droplet injection speed is set $U_{inj} = 7$ m/s. The average droplet Reynolds, Weber, and Ohnesorge numbers for this initial droplet diameter are $Re_d = U_{inj} D_{32}/\nu_{H_2O} = 194$, $We_d = \rho_{H_2O} U_{inj}^2 D_{32}/\sigma_{H_2O} = 20.7$, and $Oh_d = \sqrt{We_d}/Re_d \approx 0.0235$, respectively.

4. Results and discussion

4.1. Nonheated cylinder

Fig. 11 presents the variation of D_{32} and U with axial (streamwise) position for different radial (cross-stream) locations of $z = 0, 10$ mm, and 20 mm. The variable U is the droplet mean axial (streamwise) component of velocity. The computational and experimental results are compared, using the initial condition for the simulations of $q = 3$ and $D_{10} = 25$ μm at the nozzle exit. The experimental Type A evaluation of the standard uncertainty for D_{32} is 1.9 μm (7.4% of the mean value), and for U is 0.18 m/s (4.4% of the mean value). This uncertainty is estimated from the largest standard deviation of the mean (among standard deviations of the mean based on two replicates at each measurement location) throughout the measurement domain. The Type B evaluation is more difficult to estimate and is discussed in detail in Widmann and Presser (2002).

Fig. 11(a) shows that the value of D_{32} increases with increasing radial distance for locations upstream of the cylinder. The larger droplets have greater initial momentum and subsequently are dispersed farther in the cross-stream direction than the smaller droplets, which tend to remain near the centerline. For locations downstream of the cylinder (i.e., $x > 0$), the predictions again indicate that smaller values of D_{32} are present near the centerline, consistent with experimental measurements. Note that the experimental results for $z = 0$ and 10 mm at $x > 0$ are reversed from the expected order, which is attributed to the closeness of the values and the measurement uncertainty. Smaller droplets are more readily entrained into the air stream (their Stokes number is smaller), which indicates that these droplets are transported more readily into the recirculation zone found immediately downstream of the cylinder. Fig. 12 presents a comparison of instantaneous snapshots of the droplet field from the (a) experiments and (b) computations. The absence of observed droplets behind the cylinder in Fig. 11(a) is indicative of larger droplet transport radially outward. Regarding the droplet streamwise velocities presented in Fig. 11(b), prior to droplet impact against the cylinder wall, the droplet located in the center (i.e., $z = 0$) has a larger component of streamwise velocity than at larger radial positions. The droplets that do not impact the cylinder (i.e., $z = 20$ mm) follow the displaced streamline around the cylinder, and accelerate to approximately 45% of the far-field velocity and then decelerate. Differences are observed between the predictions and experiments at $z = 20$ mm. These differences may be attributed to the well-known limitations of using the $k-\varepsilon$ model to predict flow separation; however, the overall recirculation zone of the air stream predicted behind the cylinder in Fig. 13 is in reasonable agreement with the large eddy simulation results of Breuer (1998)—indicating an average recirculation zone length (normalized to the cylinder diameter) of $x/D_{cyl} \approx 2.2$.

The droplet size PDF of experiment, collected at $x = 0$ and $z = 20$ mm, is plotted in Fig. 14. The result is compared with the Rosin–Rammner model and seems to be in good agreement. It is known that the droplet distribution changes downstream because of the various physical

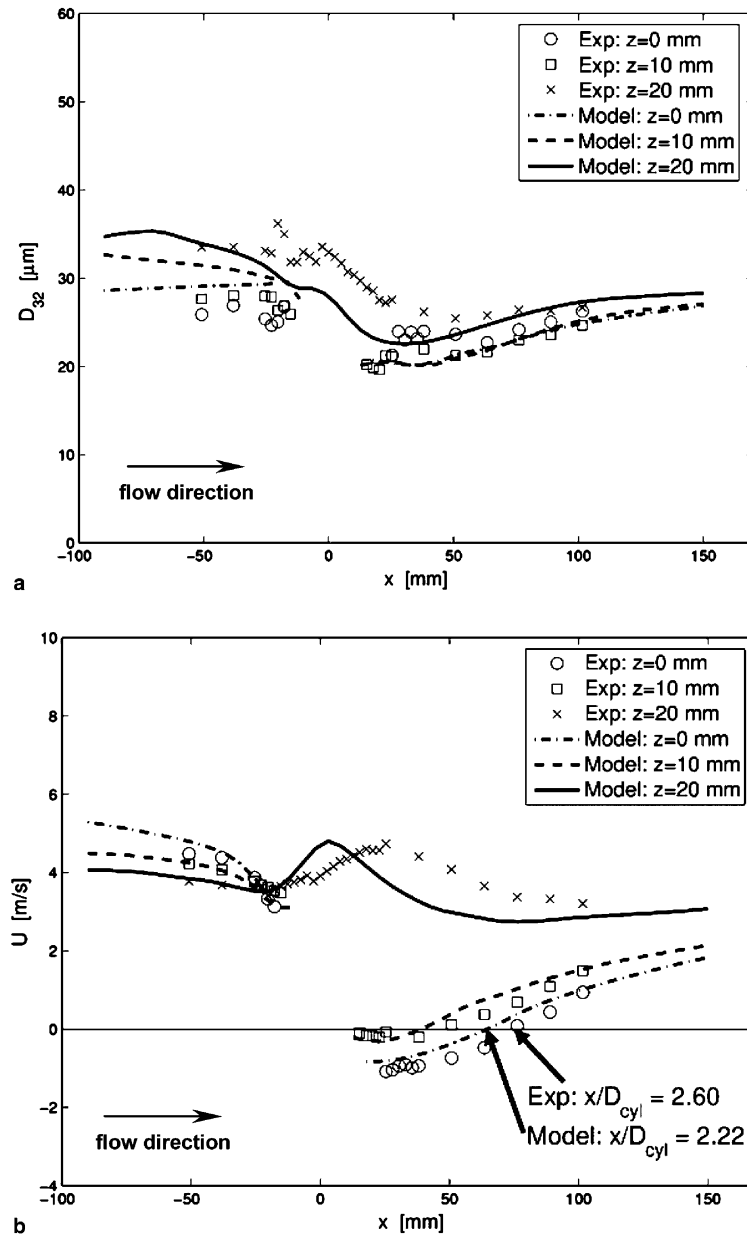


Fig. 11. Variation of the: (a) Sauter mean diameter (D_{32}) and (b) droplet mean axial (or streamwise, U) velocity with axial (or streamwise) location, x , and at different radial (or cross-stream) locations (i.e., $z = 0, 10$ mm, and 20 mm). The model results are compared against the experimental data. Note the computational results are from the unheated cylinder case.

phenomena which occur in space, such as coalescence, evaporation, and the droplet impact against the solid wall (which may lead to the production of small droplets due to shattering). Here in Fig. 14, the droplet size distribution changes slightly (i.e., from $q = 3.0$ at $x = -180$ mm to

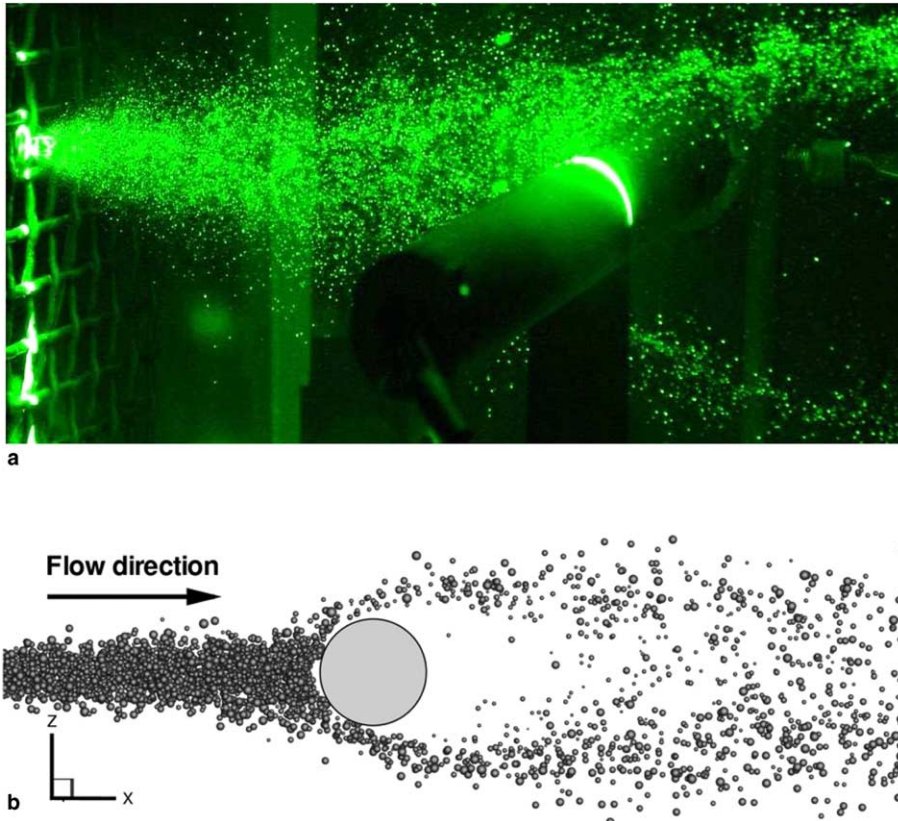


Fig. 12. View of the injected water spray over the unheated cylinder from the: (a) experiment (3D view) and (b) simulation (2D view).

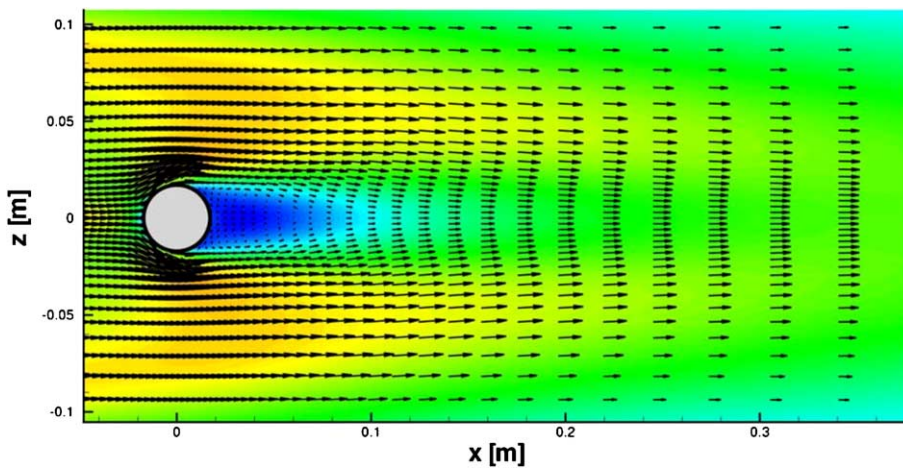


Fig. 13. Air stream velocity vectors around the cylinder at quasi-steady state. Relaxation of the velocity vectors is shown in the streamwise direction. Contour color is scaled with the magnitude of the streamwise velocity.

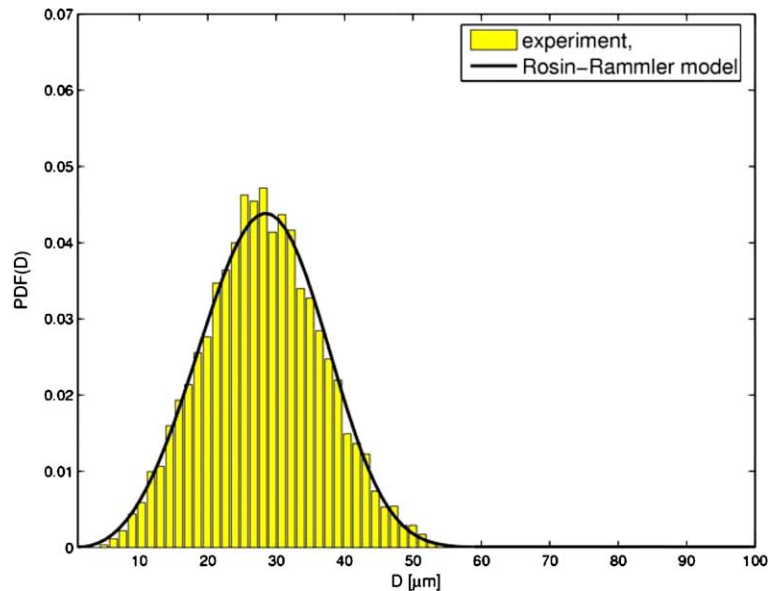


Fig. 14. Comparison between experimental data and the Rosin–Rammler model at axial location, $x = 0$ mm and the radial location, $z = 20$ mm. Note, experimental results are from the nonheated-cylinder case.

$q = 3.6$ at $x = 0$) mainly because of the droplet gradation which followed by the droplet separation (or launching) from the liquid core of the spray at the nozzle exit. Thus, the smaller droplets are entrained toward to the centerline while the larger droplets are located at larger radius (i.e., $z = 20$ mm). Consequently, the droplet distribution became more uniform due to the droplet gradation and, thus, the dispersion coefficient increased at $z = 20$ mm in the downstream location of $x = 0$.

4.2. Heated cylinder

The second case considered is the impact of the spray with a heated cylinder. For fire suppression applications, objects near a fire are heated and the characteristics of the spray during its impact with the object may be changed when the surface is at an elevated temperature. To simulate the droplet impact process, the effect of a heated surface is accounted for in the model by changing the fluid contact angle to account for changes in the wettability of the surface (see Fig. 15). The effect of heat transfer to the droplet, however, is ignored. The heating of the surface and increase in the contact angle reduces the maximum spreading diameter, β_{\max} , at state (2), as shown in Fig. 6 (also see Pasandideh-Fard et al., 1996; Chandra and Avedisian, 1991).

When the contact angle increases, the probability of droplets rebounding increases, and therefore a greater number of larger droplets that would normally stick to the surface at low temperatures rebound and are entrained by the flow. In addition, the heat transfer from the hot cylinder to the surrounding gas will quickly vaporize the smaller droplets (see the water vapor downstream of the heated cylinder surface in Fig. 16). The combined effects of wettability and heat transfer then are expected to result in an overall increase in droplet mean diameter. Fig. 17 presents the

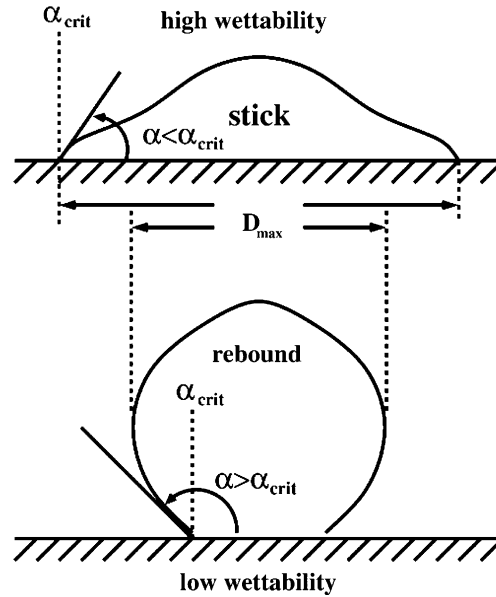


Fig. 15. Schematic illustrating sticking and rebounding of a droplet in contact with a surface. The criteria between sticking and rebounding are set by the critical contact angle. The surface with higher wettability has a smaller contact angle. The surface condition (such as its roughness and temperature) changes the state of its wettability.

variation of the droplet mean (a) diameter and (b) velocity with axial position at $z = 20$ mm for the unheated and heated cylinders. Heating of the cylinder results in an increase in the value of D_{32} , as compared to the case without heating, based on the modeling results. However, the



Fig. 16. View of the injected water spray over the heated cylinder.

experimental data appears to exhibit the opposite trend, with heating resulting in a lower mean diameter. The reason for this apparent contradiction is that in the simulations, heating of the droplet at impact is not explicitly taken into account. Heating from the cylinder will have a greater

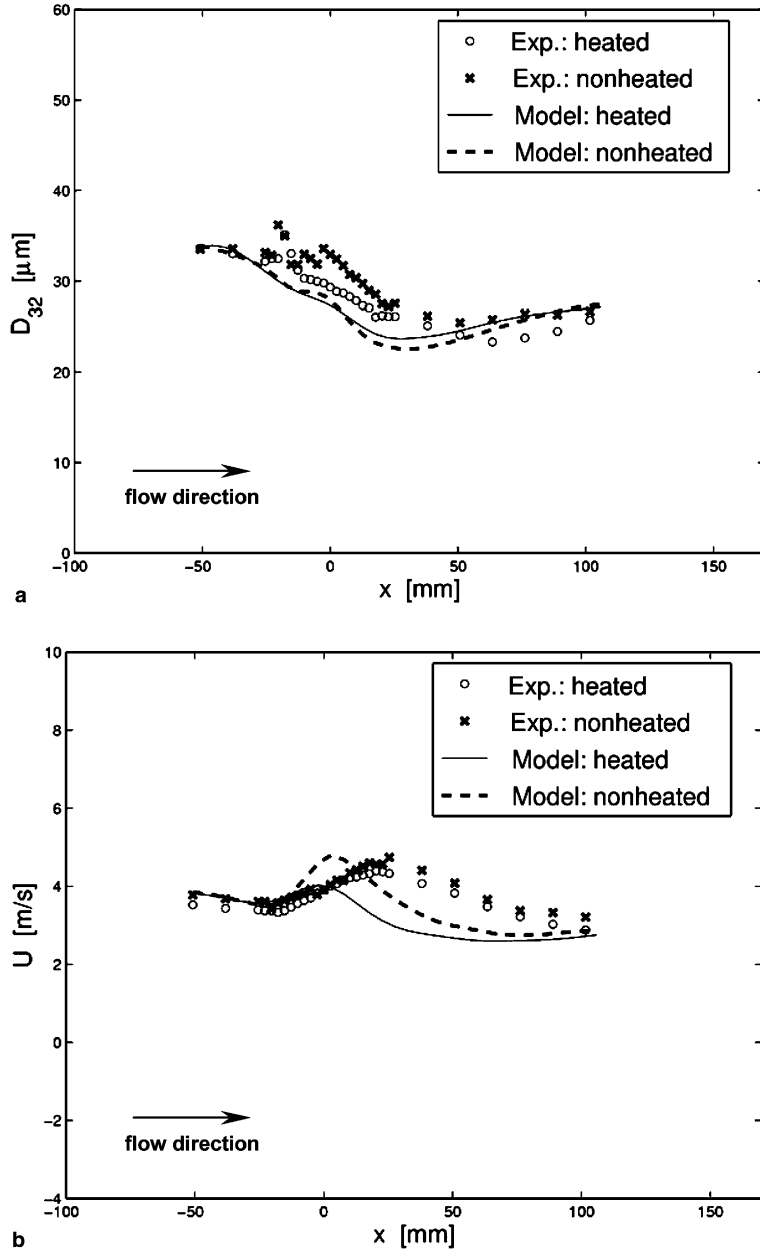


Fig. 17. Variation of the Sauter mean diameter (D_{32}) and droplet mean axial (or streamwise, U) velocity with axial position, x , at $z = 20$ mm. Results are compared for the heated and unheated cylinder cases.

effect on droplet vaporization than the unheated cylinder, and thus results in an overall decrease in droplet mean size. Efforts to examine and model the effects of droplet heating during impact will be undertaken in the future but are outside the scope of the present study. The increase in

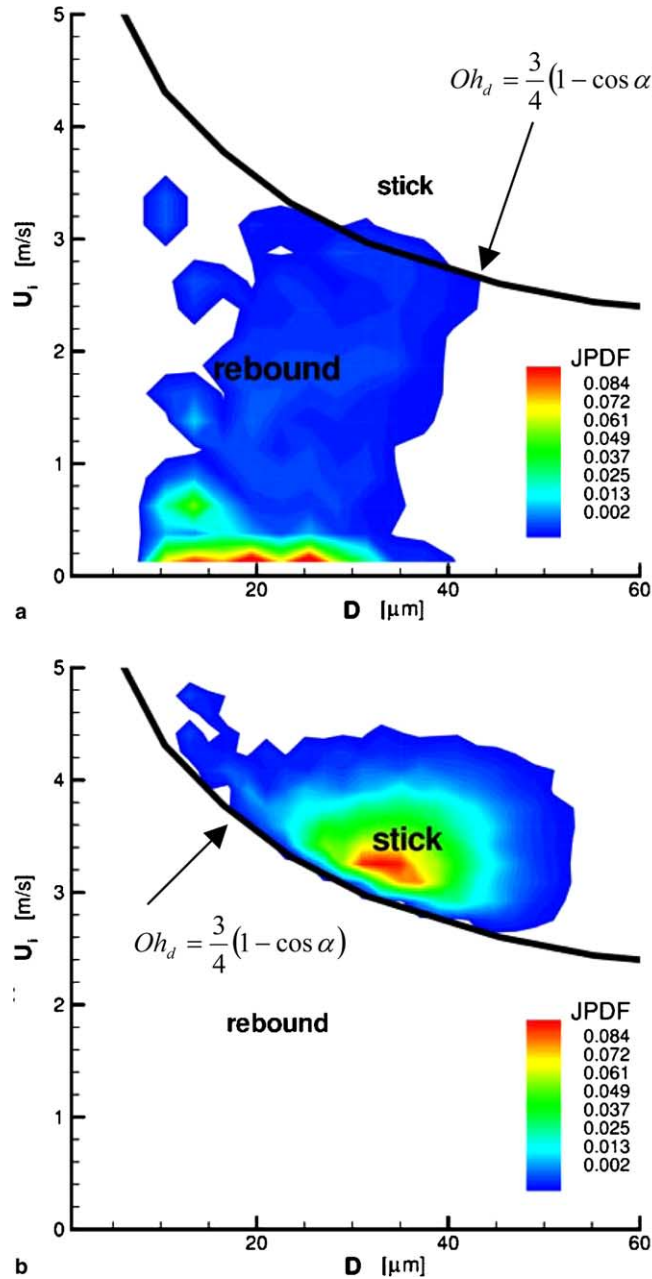


Fig. 18. Droplet velocity-size joint probability distribution functions (JPDF) of the: (a) rebounding and (b) sticking droplets for the heated-cylinder case. Statistics were collected at the impacting surface of the cylinder.

Table 1
Statistics of rebounding and sticking droplets for the heated cylinder case

| | Rebounding droplets | Sticking droplets |
|--------------------------------|----------------------------|----------------------------|
| Total droplet number | 2,144,625 | 6,232,085 |
| Total mass during 2 s duration | 1.599×10^{-5} kg | 1.585×10^{-4} kg |
| Average mass per droplet | 7.456×10^{-12} kg | 2.543×10^{-11} kg |
| Average diameter | 24.24 μm | 36.50 μm |

contact angle from heating also increases the rebounding kinetic energy ($E_{\text{KE}}^{(3'')}$) from Eq. (8), and results in a higher droplet rebound velocity. However, it should be reminded that only a few droplets were found rebounding for the unheated case while there were a relatively larger number of rebounding droplets for the heated case. For the unheated case, the majority of the droplets in contact with the cylinder were sticking (rather than rebounding) and, therefore, the overall droplet momentum was less influenced by the momentum loss of the rebounding phenomenon. In addition, the accelerated droplets around the cylinder essentially dominated the overall droplet momentum. For this reason, the overall droplet velocity for the unheated case is larger than that for the unheated case, as shown in Fig. 17(b).

To further explore the likelihood of droplets rebounding off or sticking to the surface of the heated cylinder, the probability of droplet rebounding and sticking is summarized in Table 1. Fig. 18 presents the joint probability distribution function (JPDF), based on the correlation between U_i and D , for droplet (a) rebounding and (b) sticking. The occurrence of the sticking droplets is about 2.9 times more abundant than rebounding droplets among the droplets that impact the cylinder. Droplet sticking is also generally associated with the larger droplets (also refer to Fig. 8). The total liquid mass injected during the 2 s spray injection time is 0.00168 kg, of which 1.0% is in rebounding droplets and 9.42% in sticking droplets. The rest of the mass (i.e., 89.63%) is in droplets that are transported around the cylinder. Equating Eqs. (2) and (4) may be used to develop a criterion that separates the rebounding and sticking regimes, and is expressed as

$$Oh_d = \frac{3}{4}(1 - \cos \alpha) \quad (16)$$

This criterion is drawn as a curve in Fig. 18 for the range of $5 \mu\text{m} < D < 60 \mu\text{m}$ and $0 < U_i < 5$ m/s. When the droplet velocity is above the critical line then the droplet sticks to the cylinder surface, otherwise it bounces off the surface. As shown in Fig. 18(a), while there is a broad range in velocity and sizes that result in droplet rebounding, the most frequent occurrences are found for $D = 25.5 \mu\text{m}$ and $U_i = 0.125$ m/s, probably indicative of droplets that rebound a second (or third) time. This implies that the total number of droplets rebounding may be somewhat lower than indicated by the statistics since some may be counted more than once. Fig. 18(b) shows that the range in droplet size and velocity is narrower for the sticking droplets with the highest occurrence corresponding to $D = 33 \mu\text{m}$ and $U_i = 3.25$ m/s.

5. Conclusions

Transport of a water spray over a circular cylinder in a turbulent flow field for the fire-suppression applications is simulated using a stochastic separated flow technique that includes sub-

models for droplet dynamics, heat and mass transfer due to evaporation, and a newly developed wall-impact model. Results using this model show good agreement to experimental measurements of droplet mean size and velocity around the cylinder. Discrepancies in the prediction of droplet size and velocity around the cylinder for the unheated case are attributed to the limitations of the current RANS turbulence model. A detailed analysis of droplet impact for a heated cylinder reveals that 10% of the total spray mass impacts the cylinder, of which most of this mass is associated with droplet sticking. Finally, an Oh_d -based criterion is developed to demarcate droplet rebounding and sticking from the correlation of U_i and D . Future work will examine extending the current model and the U_i - D impact regime map to include the effects of droplet shattering.

Acknowledgements

Sandia is a multiprogram laboratory operated by Sandia Corporation, a Lockheed Martin Company for the United States Department of Energy's National Nuclear Security Administration under contract DE-AC04-94AL85000. The first author acknowledges that this research was conducted during his presence at Sandia National Laboratories. The second author acknowledges the support of National Science Foundation under Grant No. CTS-0348110. The third author wishes to acknowledge the partial support of this research by the Department of Defense Next Generation Fire Suppression Technology Program, funded by the DoD Strategic Environmental Research and Development Program. He also would like to acknowledge Dr. George Papadopoulos who took the pictures of the spray impinging on the cylinder.

References

- Aziz, S.D., Chandra, S., 2000. Impact, recoil and splashing of molten metal droplets. *Int. J. Heat Mass Transfer* 43, 2841–2857.
- Babinsky, E., Sojka, P.E., 2002. Modeling drop size distributions. *Progress Energy Combust. Sci.* 28, 303–329.
- Bachalo, W.D., Houser, M.J., 1984. Development of the phase/doppler spray analyzer for liquid droplet size and velocity characterizations. In: *Proceedings of the AIAA/SAE/ASME 20th Joint Propulsion Conference*, Cincinnati, OH, June.
- Bai, C.X., Rusche, H., Gosman, A.D., 2002. Modeling of gasoline spray impingement. *Atomizat. Sprays* 12, 1–27.
- Bernardin, J.D., Mudawar, I., Walsh, C.B., Franses, E.I., 1997. Contact angle temperature dependence for water droplets on practical aluminum surfaces. *Int. J. Heat Mass Transfer* 40, 1017–1033.
- Breuer, M., 1998. Larger eddy simulation of the subcritical flow past a circular cylinder: numerical and modeling aspects. *Int. J. Numer. Methods Fluids* 28, 1281–1302.
- Chandra, S., Avedisian, C.T., 1991. On the collision of a droplet with a solid surface. *Proc. R. Soc. Lond. A* 432, 12–41.
- Chhabra, R.P., Agarwal, L., Sinha, N.K., 1999. Drag on non-spherical particles: an evaluation of available methods. *Powder Technol.* 101, 288–295.
- DesJardin, P.E., Gritzo, L.A., 2002. A dilute spray model for fire simulations: formulation, usage and benchmark problems. Sandia National Laboratories Technical Report, No. SAND2002-3419, Albuquerque.
- DesJardin, P.E., Presser, C., Disimile, P.J., Tucker, J.R., 2002. A droplet impact model for agent transport in engine nacelles. In: *Proceedings of the Halon Options Technical Working Conference (HOTWC)*.
- DesJardin, P.E., Presser, C., Disimile, P.J., Tucker, J.R., 2003. A phenomenological droplet impact model for lagrangian spray transport, In: *AIAA Paper 2003-1322, 41st AIAA Aerospace Sciences Meeting and Exhibition*.
- Faeth, G.M., 1983. Evaporation and combustion in sprays. *Progress Energy Combust. Sci.* 9, 1–76.

- Faeth, G.M., 1987. Mixing, transport and combustion in sprays. *Progress Energy Combust. Sci.* 13, 293–345.
- Foote, G.B., 1975. The water drop rebound problem: dynamics of collision. *J. Atmosph. Sci.* 32 (2), 390–402.
- Ford, R.E., Furmidge, C.G.L., 1967. Impact and spreading of spray drops on foliar surfaces. In: *Wetting, S.C.I. (Ed.), Monograph No. 25. Society of Chemical Industry*, pp. 417–432.
- Fukumoto, M., Nishioka, E., Nishiyama, T., 2002. New criterion for splashing in flattening of thermal sprayed particles onto flat substrate surface. *Surf. Coat. Technol.* 161, 103–110.
- Ganser, G.H., 1993. A rational approach to drag prediction of spherical and nonspherical particles. *Powder Technol.* 77, 143–152.
- Gentner, F., Rioboo, R., Baland, J.P., Coninck, J., 2004. Low inertia impact dynamics for nanodrops. *Langmuir* 20, 4748–4755.
- Harlow, F.H., Shannon, J.P., 1967. The splash of a liquid drop. *J. Appl. Phys.* 38, 3855–3866.
- Harvie, D.J.E., Fletcher, D.F., 2001. A hydrodynamic and thermodynamic simulation of droplet impacts on hot surfaces, Part I: theoretical model. *Int. J. Heat Mass Transfer* 44, 2633–2642.
- Healy, W.M., Hartley, J.G., Abdel-Khalik, S.I., 1996. Comparison between theoretical models and experimental data for the spreading of liquid droplets impacting a solid surface. *Int. J. Heat Mass Transfer* 39, 3079–3082.
- Helenbrook, B.T., Edwards, C.F., 2002. Quasi-steady deformation and drag of uncontaminated liquid drops. *Int. J. Multiphase Flow* 28, 1631–1657.
- Jones, W.P., Launder, B.E., 1972. The prediction of laminarization with a two-equation model of turbulence. *Int. J. Heat Mass Transfer* 15, 301–314.
- Kim, H.Y., Feng, Z.C., Chun, J.H., 2000. Instability of a liquid jet emerging from a droplet upon collision with a solid surface. *Phys. Fluids* 12, 531–541.
- Kim, H.Y., Park, S.Y., Min, K., 2003. Imaging the high-speed impact of microdrop on solid surface. *Rev. Scient. Instrum.* 74, 4930–4937.
- Manzello, S.L., Yang, J.C., 2004. An experimental investigation of water droplet impingement on a heated wax surface. *Int. J. Heat Mass Transfer* 47, 1701–1709.
- Mao, T., Kuhn, D., Tran, H., 1997. Spread and rebound of liquid droplets upon impact on flat surfaces. *AIChE J.* 43 (9), 2169–2179.
- Maxey, M.R., Riley, J.J., 1983. Equation of motion for a small rigid sphere in a non-uniform flow. *Phys. Fluids* 26, 883–889.
- Mehdizadeh, N.Z., Chandra, S., Mostaghimi, J., 2004. Formation of fingers around the edges of a drop hitting a metal plate with high velocity. *J. Fluid Mech.* 510, 353–373.
- Moita, A.S.H., Moreira, A.L.N., 2003. Influence of surface properties on the dynamic behavior of impacting droplets. In: *Proceedings of the 9th International Conference on Liquid Atomization and Spray Systems*, July, 2003.
- Mundo, C., Sommerfeld, M., Tropea, C., 1995. Droplet-wall collisions: experimental studies of the deformation and breakup process. *Int. J. Multiphase Flow* 21 (2), 151–173.
- Mundo, C., Sommerfeld, M., Tropea, C., 1998. On the modeling of liquid sprays impinging on surfaces. *Atomizat. Sprays* 8, 625–652.
- Park, K., Watkins, A.P., 1996. Comparison of wall spray impaction models with experimental data on drop velocities and sizes. *Int. J. Heat Fluid Flow* 17, 424–438.
- Pasandideh-Fard, M., Qiao, Y.M., Chandra, S., Mostaghimi, J., 1996. Capillary effects during droplet impact on a solid surface. *Phys. Fluids* 7, 236–247.
- Patankar, S.V., 1980. *Numerical Heat Transfer and Fluid Flow*. Taylor and Francis, New York.
- Pope, S.B., 2000. *Turbulent Flows*. Cambridge, United Kingdom (Chapter 6).
- Presser, C., Widmann, J.F., DesJardin, P.E., Gritzo, L.A., 2001. Measurements and numerical predictions of liquid agent dispersal around solid obstacles. In: *Proceedings of the 11th Halon Options Technical Working Conference (HOTWC-2001)*, New Mexico Engineering Research Institute, Albuquerque, NM, pp. 122–130.
- Presser, C., Widmann, J.F., Papadopoulos, G., 2002. Liquid agent transport around solid obstacles. In: *Gann, R.G., Reneke, P.A. (Eds.), Proceedings of the 12th Halon Options Technical Working Conference (HOTWC-2002)*, NIST Special Publication 984. NIST, Gaithersburg, MD.
- Roisman, I.V., Prunet-Foch, B., Tropea, C., Vignes-Adler, M., 2002. Multiple drop impact onto a dry solid substrate. *J. Colloid Interface Sci.* 256, 396–410.

- Schmehl, R., Roskamp, H., Willmann, M., Wittig, S., 1999. CFD analysis of spray propagation and evaporation including wall film formation and spray/film interactions. *Int. J. Heat Fluid Flow* 20, 520–529.
- Snyder, W.H., Lumley, J.L., 1971. Some measurements of particle velocity autocorrelation functions in a turbulent flow. *J. Fluid Mech.* 48, 41–71.
- Taylor, B.N., Kuyatt, C.E., 1994. Guidelines for evaluating and expressing the uncertainty of NIST measurement results, NIST Technical Note 1297, National Institute of Standards and Technology, Gaithersburg, MD.
- Wachters, L.H., Westerling, N.A.J., 1966. The heat transfer from a hot wall to impinging water drops in the spherical state. *Chem. Eng. Sci.* 21, 1047–1056.
- Wang, M., Watkins, A.P., 1993. Numerical modeling of diesel spray wall impaction phenomena. *Int. J. Heat Fluid Flow* 14, 301–312.
- Wells, M.R., Stock, D.E., 1983. The effects of crossing trajectories on the dispersion of particles in a turbulent flow. *J. Fluid Mech.* 136, 31–62.
- Widmann, J.F., Presser, C., 2002. A benchmark experimental database for multiphase combustion model input and validation. *Combust. Flame* 129, 47–86.
- Worthington, A.M., 1908. *A Study of Splashes*. Longmans & Green, London.
- Yoon, S.S., Hewson, J.C., DesJardin, P.E., Glaze, D.J., Black, A.R., Skaggs, R.R., 2004. Numerical modeling and experimental measurements of a high speed solid-cone water spray for use in fire suppression applications. *Int. J. Multiphase Flow* 30, 1369–1388.